

Colloidal nanoelectronic state machines based on 2D materials for aerosolizable electronics

Volodymyr B. Koman¹, Pingwei Liu^{1,2}, Daichi Kozawa¹, Albert Tianxiang Liu¹, Anton L. Cottrill¹, Youngwoo Son¹, Jose A. Lebron¹ and Michael S. Strano^{1*}

A previously unexplored property of two-dimensional electronic materials is their ability to graft electronic functionality onto colloidal particles to access local hydrodynamics in fluids to impart mobility and enter spaces inaccessible to larger electronic systems. Here, we demonstrate the design and fabrication of fully autonomous state machines built onto SU-8 particles powered by a two-dimensional material-based photodiode. The on-board circuit connects a chemiresistor circuit element and a memristor element, enabling the detection and storage of information after aerosolization, hydrodynamic propulsion to targets over 0.6 m away, and large-area surface sensing of triethylamine, ammonia and aerosolized soot in inaccessible locations. An incorporated retroreflector design allows for facile position location using laser-scanning optical detection. Such state machines may find widespread application as probes in confined environments, such as the human digestive tract, oil and gas conduits, chemical and biosynthetic reactors, and autonomous environmental sensors.

Two-dimensional (2D) materials, such as graphene and transition metal dichalcogenides, can be fashioned into novel planar circuit elements, including photodiodes¹, transistors², chemiresistor sensors³, memory elements⁴ and capacitors^{5,6}. This has enabled the transfer and construction of nanoelectronic circuits grafted onto unique surfaces. However, one surface that has yet to be explored for this purpose is a fluid dispersible colloid. This could extend nanoelectronics to remote and inaccessible spaces and volumes. As on-board circuit elements increase in number and complexity, access independent sources of power, and manifest input and output information sources, a threshold is reached where the colloid constitutes a finite-state machine or computational device for handling informational flows.

Nanofabrication and synthesis methods have allowed researchers to create sophisticated colloidal devices (single particles or assemblies that serve a particular function), but not ones possessing autonomous circuitry, logic manipulation or information storage. In particular, state-of-the-art multifunctional micro/nanoparticles do not process information in an autonomous way when decoupled from their environment^{7,8}. Similarly, conceptual devices referred to as ‘molecular machines’ rely on the stochastic thermodynamics of their environment⁹ (for example, the Brownian ratchet). Directed self-assembly methods are still in their infancy and are only able to create rather simple geometries—and not yet autonomous function^{10,11}; on the other hand, nanoelectronics has enabled several state machine implementations, although not in the form of autonomous colloidal particles^{12–14}. DNA electronics has been proposed in ref. ¹⁵, but the formation of electronic, DNA-based, colloidal state machines has not been realized. Finally, there has been recent progress in creating so-called ‘biorobots’, or biological state machines (a natural organism whose genome has been modified to manifest diverse, non-natural functions)^{16–18}. However, biorobots can only exist under specific biological conditions, requiring limitations to the environment, temperature, pH and salinity, and protection against wild-type organisms. This constrains the envisioned applications compared to purely synthetic state machines, which could

bring both digital and analog electronics to harsh environments in a scalable way. For example, the large-area monitoring of environmental bacteria, biological spores, particulates and volatile organic compounds (VOCs) requires significant resources¹⁹ that could be more efficiently deployed using synthetic state machines (Supplementary Note 1).

The concept of cubic millimetre-sized devices, previously called ‘smart dust’, was not implemented for fluid dispersion, but nevertheless constituted an early attempt towards achieving miniaturized autonomous electronics²⁰. However, it is clear that the power density limits further downward scaling. Batteries with typical energy capacities up to $0.1 \text{ nW } \mu\text{m}^{-3}$ (ref. ²¹) and with power harvesting techniques that can deliver between 0.1 and $10 \text{ nW } (10^4 \text{ } \mu\text{m}^2)^{-1}$ (ref. ^{22–24}) remain insufficient for conventional electronics at the microscale (Supplementary Note 2). Fortunately, 2D material devices are predicted to bypass these difficulties²⁵ because they have a number of advantages²⁶, such as low-power performance compared to Si ($<0.5 \text{ V}$), acceptable gate control with subthreshold swings $\ll 60 \text{ mV dec}^{-1}$, and large turn-on currents ($> 10^3 \text{ } \mu\text{A } \mu\text{m}^{-1}$).

In this work we create a new class of submillimetre colloidal particles with 2D electronic materials (graphene, hexagonal boron nitride (hBN), MoS_2 and WSe_2) grafted onto them. Top-down fabrication can pattern them into functional electronic circuits, transistors, memory and sensors, creating what we call colloidal state machines (CSMs), or particles capable of collecting, manipulating and storing information autonomously. Such CSMs can access local fluid hydrodynamics to enter spaces inaccessible to conventional electronics. Our designs include circuits with 2D material p–n heterojunctions of MoS_2 and WSe_2 , powering MoS_2 chemiresistor circuit elements. Such CSMs can be aerosolized and detect VOCs or carbon nanoparticulates along their trajectories, storing the detection in a non-volatile memristor device consisting of a Au– MoS_2 –Ag junction shielded from the environment by an inert hBN monolayer. These state machines exploit a unique property of 2D electronic materials in their ability to impart fundamentally new functions to highly mobile colloids. We demonstrate several specific

¹Department of Chemical Engineering, Massachusetts Institute of Technology, Cambridge, MA, USA. ²State Key Lab of Chemical Engineering, College of Chemical and Biological Engineering, Zhejiang University, Hangzhou, China. *e-mail: strano@mit.edu

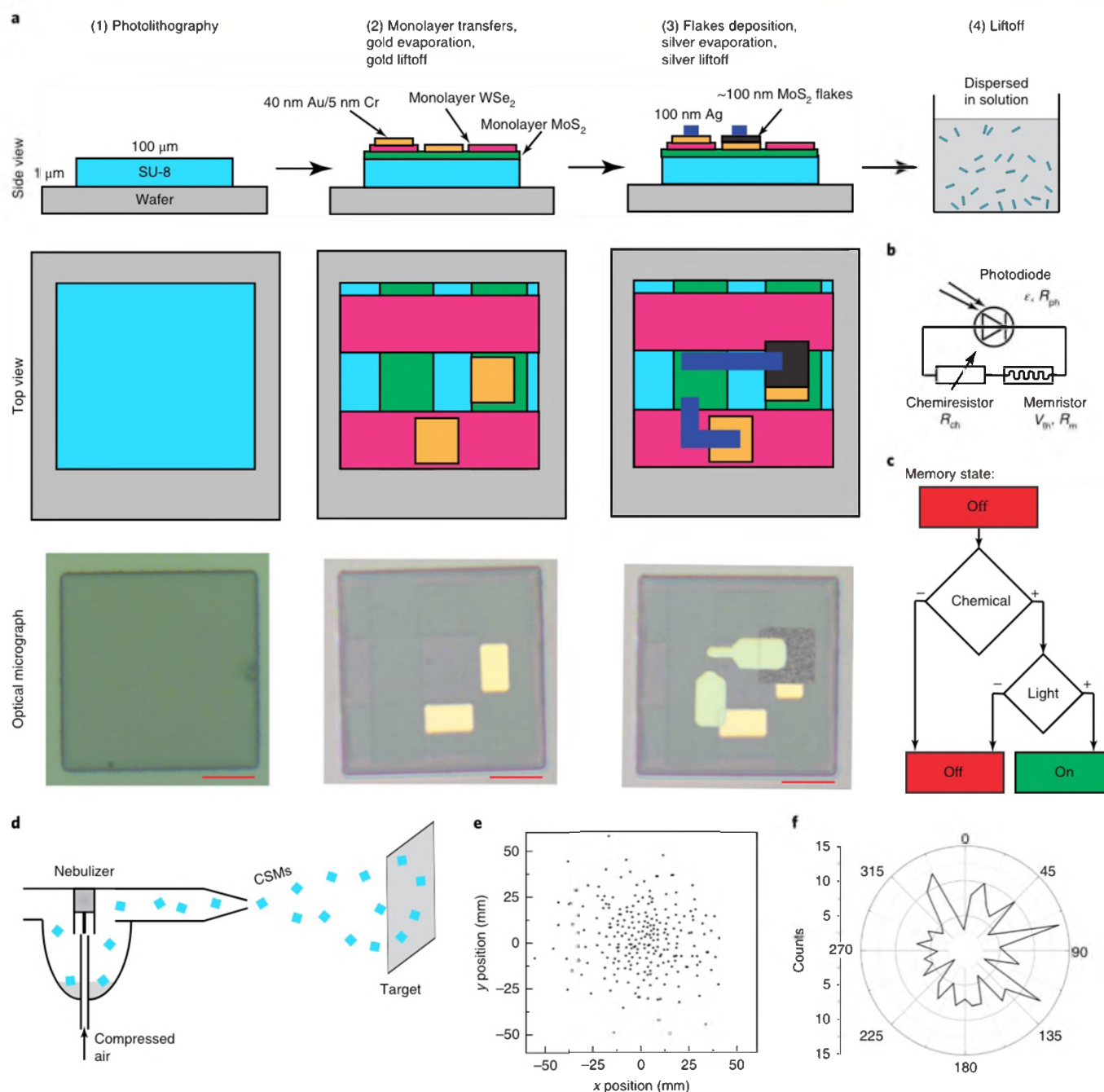


Fig. 1 | CSM fabrication and aerosolization. **a**, Summary of CSM fabrication steps with side and top view schematics and top view optical micrographs: (1) SU-8 base fabrication; (2) MoS₂ and WSe₂ monolayer transfer with gold evaporation to form photodiodes; (3) MoS₂ flakes transfer to form memristors, while silver evaporation forms electrical contacts for the MoS₂ chemiresistor; (4) CSMs are released from the wafer by liftoff and are stored as a dispersion. Scale bars, 25 μm . **b**, Electrical circuit diagram of CSM. The photodiode converts light into current (generating voltage ϵ and with internal resistance R_{ph}), which turns on the memristor (with a threshold voltage V_{th} and internal resistance R_m) only if the chemiresistor detects an analyte (resistance R_{ch}). **c**, Block diagram for the CSM state machine. The initial memory state off changes to on only in the presence of both chemical and light signals. **d**, CSM dispersion is aerosolized using a nebulizer with 4–10 m s^{-1} speed across 0.6 m distance in air. **e**, Digitized positions of aerosolized CSMs collected on the target. **f**, Angle distribution diagram extracted from **e** shows that the CSMs have no preferential direction.

applications, such as remote sensing of ammonia in constricted pipelines, as well as large-area sensing of aerosolized soot via stand-off deployment and retrieval of surface-dispersed state machines.

Because of their high aspect ratio, micrometre-scale 2D materials have low mechanical stability (necessary to sustain off-substrate applications). To circumvent this, we first designed a CSM base that plays the role of a carrier substrate for the 2D devices. We chose the photoresponsive polymer SU-8, as it can be processed with micrometre

precision via conventional photolithography, becomes mechanically and chemically stable after cross-linking, even during various fabrication stages (Supplementary Fig. 1), and has a smooth surface (Supplementary Fig. 2). We also designed an electrical state machine with functional elements of combinational logic on this polymer base (Fig. 1a). Specifically, this has three components—a power source, a switch and a memory element—implemented by a photodiode, chemiresistor and memristor, respectively (Fig. 1b). The photodiode

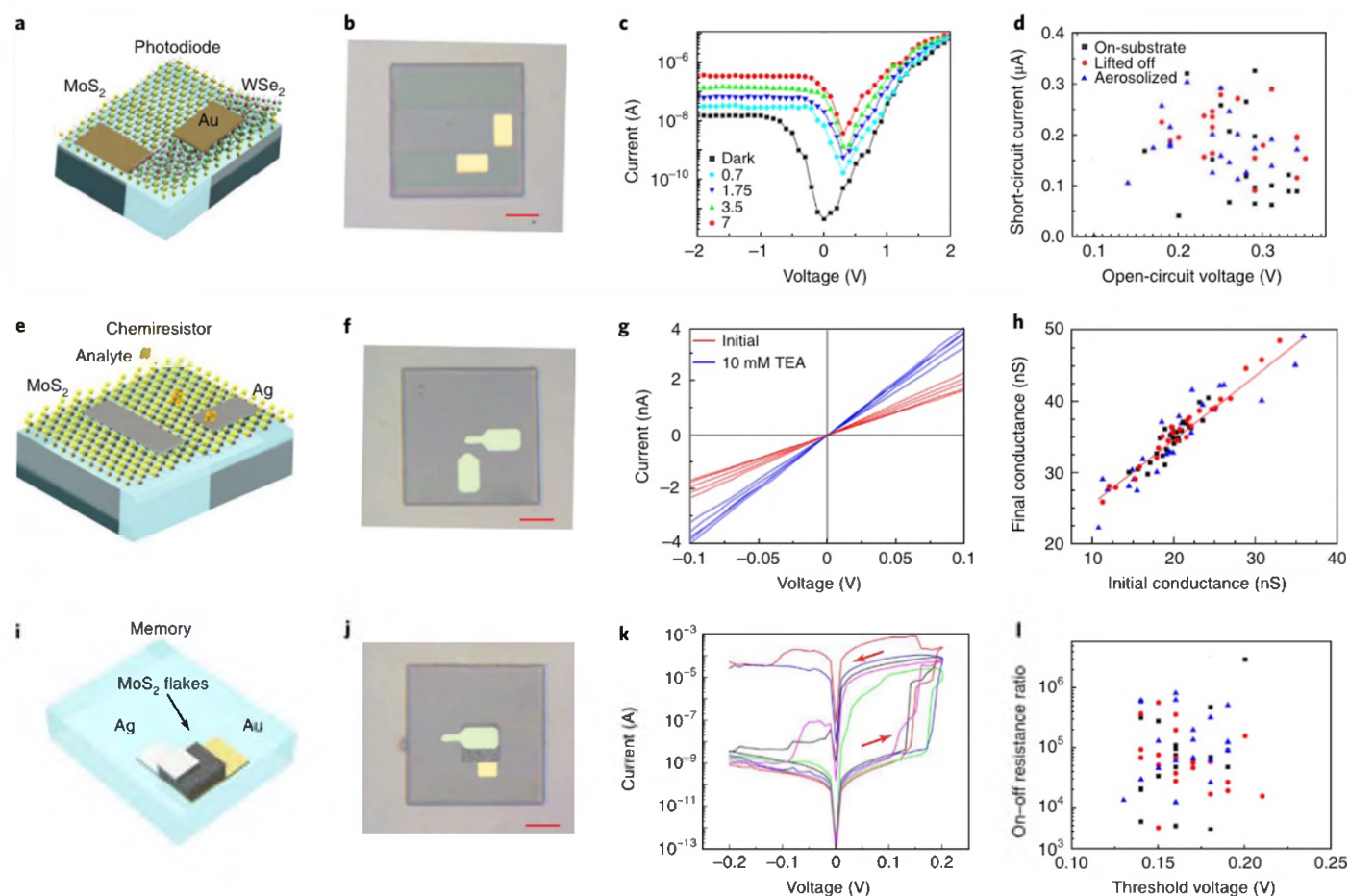


Fig. 2 | Individual components of CSM. **a, b.** Diagram (**a**) and optical image (**b**) of CSM with a photodiode fabricated from a continuous MoS_2 monolayer and $25\text{ }\mu\text{m}$ striped monolayer of WSe_2 . **c.** Typical current–voltage characteristics of a p–n photodiode composed of MoS_2 and WSe_2 monolayers under illumination by a 532 nm laser (black, in the dark; cyan, blue, green and red, under 0.7, 1.75, 3.5 and $7\text{ }\mu\text{W}\text{ }\mu\text{m}^{-2}$ illumination intensities, respectively). **d.** Master plot for multiple devices, as in **c**. Both open-circuit voltage and short-circuit current are preserved after liftoff ($\epsilon = 0.27 \pm 0.05\text{ V}$, $I_{\text{sh}} = 0.20 \pm 0.01\text{ }\mu\text{A}$) and aerosolization ($\epsilon = 0.24 \pm 0.05\text{ V}$, $I_{\text{sh}} = 0.19 \pm 0.01\text{ }\mu\text{A}$) as compared to the original on-substrate devices ($\epsilon = 0.27 \pm 0.06\text{ V}$, $I_{\text{sh}} = 0.15 \pm 0.01\text{ }\mu\text{A}$) for $N = 20$ random devices. **e, f.** Diagram (**e**) and optical image (**f**) of a CSM with a chemiresistor. **g.** Current–voltage curves for a monolayer MoS_2 chemiresistor before (red) and after (blue) the addition of 10 mM TEA. **h.** Master plot for multiple devices, as in **g**. The red line is a guide for the eye. Conductance increase: from $19.8 \pm 2.3\text{ nS}$ to $G_{\text{ch}}^{\text{f}} = 34.7 \pm 2.8\text{ nS}$ for devices on the substrate; from $G_{\text{ch}}^{\text{in}} = 21.1 \pm 5.5\text{ nS}$ to $G_{\text{ch}}^{\text{f}} = 36.1 \pm 5.5\text{ nS}$ for lifted-off devices from $G_{\text{ch}}^{\text{in}} = 20.5 \pm 6.6\text{ nS}$ to $G_{\text{ch}}^{\text{f}} = 35.0 \pm 6.4\text{ nS}$ for aerosolized devices ($N = 20$). **i, j.** Diagram (**i**) and optical image (**j**) of a CSM with a memristor. **k.** Current–voltage characteristics for a MoS_2 memristor sandwiched between gold and silver electrodes. **l.** Master plot for multiple devices, as in **k**. Both the threshold voltage and initial conductance are preserved: $V_{\text{th}} = 0.16 \pm 0.02\text{ V}$, $G_{\text{m}}^{\text{off}} = 13.4 \pm 4.0\text{ nS}$ on the silicon; $V_{\text{th}} = 0.17 \pm 0.02\text{ V}$, $G_{\text{m}}^{\text{off}} = 18.4 \pm 8.4\text{ nS}$ for lifted off device; $V_{\text{th}} = 0.17 \pm 0.02\text{ V}$, $G_{\text{m}}^{\text{off}} = 14.4 \pm 6.9\text{ nS}$ for aerosolized CSMs. In **d**, **h** and **l**, black denotes as-fabricated devices, red denotes lifted off devices, and blue denotes devices dispersed with a nebulizer. Scale bars, $25\text{ }\mu\text{m}$.

is built on a p–n heterojunction of MoS_2 and WSe_2 monolayers. Another MoS_2 monolayer serves as a chemiresistor that changes its conductance following binding of external analytes. Finally, the memristor is composed of liquid-exfoliated MoS_2 flakes sandwiched between gold and silver electrodes. The fabricated particle represents a state machine with both light and analyte as inputs and the memory state as an output (Supplementary Fig. 3). It operates in the following way. The photodiode generates voltage when it is illuminated with light, the chemiresistor switches its conductance after analyte binding, and the memristor changes its state from off to on when the applied voltage from the photodiode exceeds a threshold voltage. The whole process can be represented as two IF blocks and the logic operator AND on a block diagram. The memory component only changes its state from OFF to ON if both light shines on the photodiode and the analyte binds to the chemiresistor (Fig. 1c).

The performance of an electronic device changes when it is removed from a native substrate due to the imposed stretch and strain¹⁷. Remarkably, 2D materials possess higher strain limits than

traditional III–V materials with similar size²⁸, making them more prone to surviving the transfer process. We tested the performance of devices at three stages: (1) as-fabricated on the silicon substrate; (2) after liftoff; and (3) after aerosolization using a nebulizer across a 0.6 m distance in a 0.15-m-diameter tube (Fig. 1d and Supplementary Fig. 4). In a typical nebulizer experiment, using the microscope we identified that $N = 244$ CSMs landed on the target at the opposite end of the tube. Most of the CSMs were concentrated in a 0.06-m-diameter circle and had no preferential angular direction, proving directional aerosolization (Fig. 1e, f and Supplementary Fig. 5). Droplets ejected by the nebulizer had an initial speed of $4\text{--}10\text{ m s}^{-1}$ and diameter of $<0.3\text{ }\mu\text{m}$. After liftoff and aerosolization, some CSMs were occasionally bent (37 CSMs in one particular aerosolization experiment) or aggregated (34 CSMs; Supplementary Fig. 6 and Supplementary Note 3). Numerical calculations suggest that, after nebulizer propulsion CSMs travel $\sim 3\text{ m}$ (with travel times of $<0.3\text{ s}$) before completely stopping (Supplementary Fig. 7 and Supplementary Note 4). The motion equation is given by

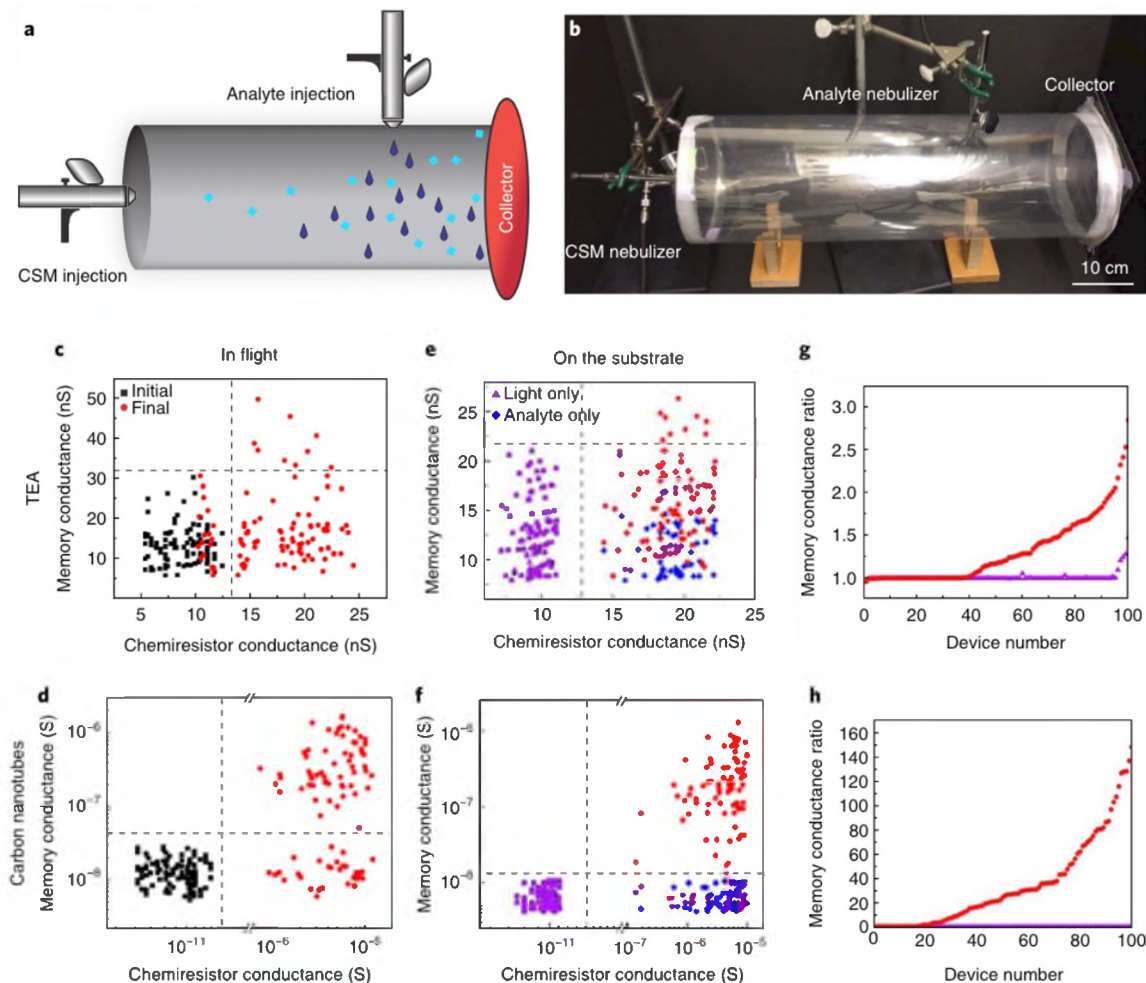


Fig. 3 | Aerosolizable electronics. **a**, Experimental schematic demonstrating remote detection and memory storage in a constrained environment: the left nebulizer injects CSMs (teal squares) across the enclosed tube injected with either TEA or aerosolized carbon nanotube particulates (dark blue droplets) using the top nebulizer. CSMs are collected on the collector, exposed to light, and their memory states are queried afterwards. **b**, Image of the experimental set-up. **c**, Chemiresistor conductance changes due to CSM exposure to TEA droplets (10 mM) during spraying, enabling memory conductance change after illumination with 532 nm laser light at $7 \mu\text{W} \mu\text{m}^{-2}$. CSMs change their chemiresistor conductance from $G_{\text{ch}}^{\text{in}} = 8.9 \pm 3.1 \text{ nS}$ to $G_{\text{ch}}^{\text{f}} = 17.3 \pm 4.1 \text{ nS}$, allowing a memristor conductance change from $G_{\text{m}}^{\text{off}} = 13.3 \pm 4.8 \text{ nS}$ to $G_{\text{m}}^{\text{on}} = 17.3 \pm 8.9 \text{ nS}$ after laser illumination (two-tailed $P = 0.0001$). Black squares denote measurements before exposure, and red circles measurements after exposure and illumination. **d**, As in **c**, but CSMs were exposed to a carbon nanotube dispersion (0.2 g l^{-1}). CSMs change their chemiresistor conductance from $G_{\text{ch}}^{\text{in}} = 8.7 \pm 2.0 \text{ pS}$ to $G_{\text{ch}}^{\text{f}} = 4.3 \pm 2.7 \mu\text{S}$, inducing a memristor conductance change from $G_{\text{m}}^{\text{off}} = 14.7 \pm 6.0 \text{ nS}$ to $G_{\text{m}}^{\text{on}} = 0.47 \pm 0.44 \mu\text{S}$. **e, f**, As in **c** and **d**, respectively, but for CSMs on-substrate. **e**, Chemiresistor conductance changed from $G_{\text{ch}}^{\text{in}} = 9.6 \pm 1.3 \text{ nS}$ to $G_{\text{ch}}^{\text{f}} = 19.1 \pm 1.9 \text{ nS}$, enabling a memristor conductance change from $G_{\text{m}}^{\text{off}} = 12.6 \pm 3.5 \text{ nS}$ to $G_{\text{m}}^{\text{on}} = 16.0 \pm 4.0 \text{ nS}$ ($P = 0.0001$); 41 CSMs did not change their memristor state (red circles). Control experiments with light showed that only 6 CSMs changed their memory state in the absence of TEA, meaning that equation (3) was not satisfied in their case. **f**, Chemiresistor conductance changed from $G_{\text{ch}}^{\text{in}} = 9.6 \pm 1.1 \text{ pS}$ to $G_{\text{ch}}^{\text{f}} = 4.9 \pm 2.9 \mu\text{S}$, inducing a memristor conductance change from $G_{\text{m}}^{\text{off}} = 12.9 \pm 3.9 \text{ nS}$ to $G_{\text{m}}^{\text{on}} = 0.50 \pm 0.49 \mu\text{S}$; 84 CSMs worked with an average memory conductance ratio of 62. Control experiments with exposure of these CSMs to only light demonstrate that no CSM changed its memristor conductance. Violet triangles denote control measurements after illumination; blue diamonds denote measurements after exposure. Dashed lines are guides for the eye. **g, h**, Ranked memory conductance ratio (ON-OFF) extracted from **e** and **f**, respectively. $N = 100$ for all experiments.

$$\frac{dv}{dt} = -\frac{3\rho_{\text{air}}}{4\rho_{\text{p}}D} v^2 C_d \quad (1)$$

where v is the particle speed, ρ_{air} and ρ_{p} are the air and particle densities, respectively, D is the particle diameter, and C_d is the particle drag coefficient. Water droplets of this size dry within 25–160 s (Supplementary Fig. 7). This hints that the droplets do not dry throughout their flight. Therefore, the presence of a water envelope possibly enhances CSM stability during landing.

2D nanoelectronics for basic state machine components

To test individual components, we constructed CSM bases with isolated devices. As a power source, we fabricated a

p–n photodiode comprised of a heterostructure of MoS_2 and WSe_2 monolayers with Au contacts in a 90° configuration and $\sim 10 \mu\text{m}$ channel length (Fig. 2a,b). Before fabrication, we performed photoluminescence, atomic force microscopy and Raman mapping measurements to confirm the continuity of the MoS_2 and WSe_2 monolayers (Supplementary Figs. 8 and 9). Following stacking, we observed the emergence of an additional photoluminescence peak at 800 nm, corresponding to the staggered gap (type II) heterostructure²⁹ (Supplementary Fig. 10). The photodiode fabricated on substrate generates photocurrent under laser illumination, reaching $\varepsilon = 0.27 \pm 0.06 \text{ V}$ open-circuit voltage and $I_{\text{sh}} = 0.15 \pm 0.01 \mu\text{A}$ short-circuit current with a 532 nm laser fluence of $P = 7 \mu\text{W} \mu\text{m}^{-2}$ (Fig. 2c), which is comparable with previous studies^{30,31}. These characteristics are

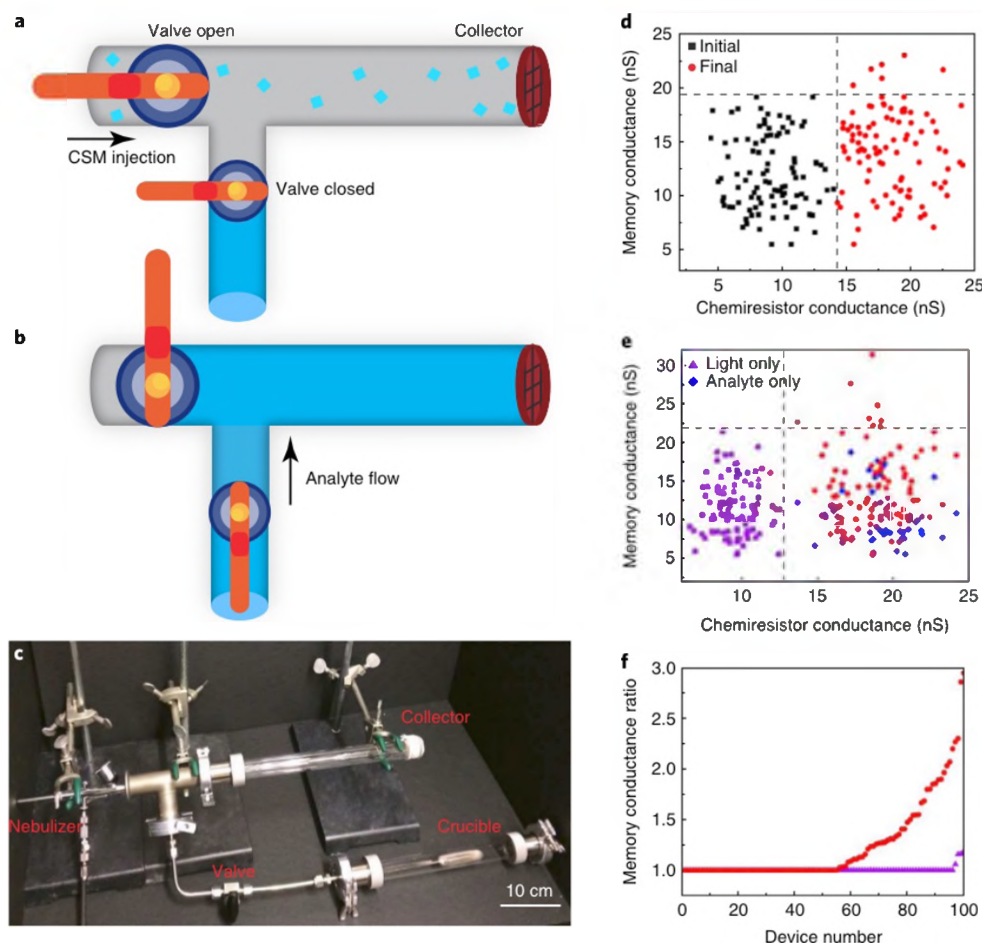
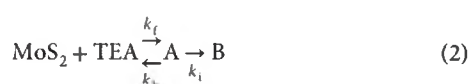


Fig. 4 | CSMs for monitoring pipeline status. **a, b**, Schematics of the pipe segment system (22 mm inner diameter), which has two separate valves for metering aerosolized CSMs (teal squares) (**a**) or ammonia (**b**). To allow for retrieval, a layer of cheesecloth served as a collector at the pipe endpoint. **c**, Image of the experimental set-up with ammonia. Once the lower valve is open, saturated ammonia vapour (~10 kPa) expands into the rest of the system. **d**, Chemiresistor conductance changes (from $G_{\text{ch}}^{\text{in}} = 9.1 \pm 2.2 \text{ nS}$ to $G_{\text{ch}}^{\text{f}} = 18.5 \pm 2.5 \text{ nS}$) due to CSM exposure to ammonia vapour, enabling a memory conductance change (from $G_{\text{m}}^{\text{off}} = 12.5 \pm 3.9 \text{ nS}$ to $G_{\text{m}}^{\text{on}} = 14.5 \pm 4.3 \text{ nS}$) after illumination with a 532 nm laser ($7 \mu\text{W} \mu\text{m}^{-2}$). Black squares and red circles denote measurements before exposure and after exposure and illumination, respectively. **e**, As in **d**, but for control CSMs on-substrate. Chemiresistor conductance changes from $G_{\text{ch}}^{\text{in}} = 9.5 \pm 1.3 \text{ nS}$ to $G_{\text{ch}}^{\text{f}} = 18.6 \pm 2.9 \text{ nS}$, enabling a memristor conductance change from $G_{\text{m}}^{\text{off}} = 11.7 \pm 3.8 \text{ nS}$ to $G_{\text{m}}^{\text{on}} = 13.7 \pm 5.0 \text{ nS}$; $P = 0.0017$. Violet triangles denote control measurements after illumination, blue diamonds denote measurements after exposure. Dashed lines are guides for the eye. **f**, Ranked memory conductance ratio extracted from **e**; 45 CSMs successfully change their memory conductance with an average ratio of 1.55. $N = 100$ for all experiments.

preserved after liftoff and aerosolization (Fig. 2d and Supplementary Fig. 11).

For the sensor element, we chose a chemiresistor design based on a MoS_2 monolayer (Fig. 2e,f). In the circuit, we designed it as a chemically induced turn-on switch to power the memristor. Mechanistically, MoS_2 increases its conductance with an analyte that demonstrates n-type doping on adsorption. An example is 10 mM triethylamine (TEA) sprayed onto MoS_2 , which results in a conductance increase (Fig. 2g,h) from $G_{\text{ch}}^{\text{in}} = 20.5 \pm 6.6 \text{ nS}$ to $G_{\text{ch}}^{\text{f}} = 35.0 \pm 6.4 \text{ nS}$ for the aerosolized elements, with similar values for on-substrate ones. To understand the reaction kinetics, we extracted the MoS_2 -TEA first-order reaction constants by analysing continuous conductance measurements of the MoS_2 chemiresistor¹²:



where binding constant $k_{\text{f}} = 0.024 \pm 0.001 \text{ s}^{-1} \mu\text{M}^{-1}$, dissociation constant $k_{\text{b}} = 0.23 \pm 0.01 \text{ s}^{-1}$ and irreversible constant $k_{\text{i}} = 0.06 \pm 0.01 \text{ s}^{-1}$, A is a physisorbed adduct of TEA and B a chemisorbed adduct (Supplementary Fig. 12 and Supplementary Note 5). The process of MoS_2 -TEA charge transfer is limited by the surface coverage, providing the maximum of 95% of MoS_2 resistance change¹³. This signifies that TEA can irreversibly bind to MoS_2 in less than 0.3 s—similar timescales to the flying time of CSMs.

To store the detection event, we designed a memristor based on MoS_2 flakes sandwiched between two different-workfunction metals. Most memristors operate in the 1–3 V range, exceeding the photodiode voltage generation of the CSM^{34–36}. However, following recent work¹⁷, a MoS_2 memristor fabricated between Au and Ag electrodes (Fig. 2i,j) with dimensions of $25 \times 25 \times 0.1 \mu\text{m}^3$ has a turn-on voltage of ~0.15 V, 100 MΩ starting resistance and its on-off ratio can reach millions (Fig. 2k and Supplementary Fig. 13e). Mechanistically, an ultrathin MoOx layer forms on the MoS_2 surface with subsequent charge trapping/detrapping at the Ag/ MoOx interface³⁷. These memristors, written to various states

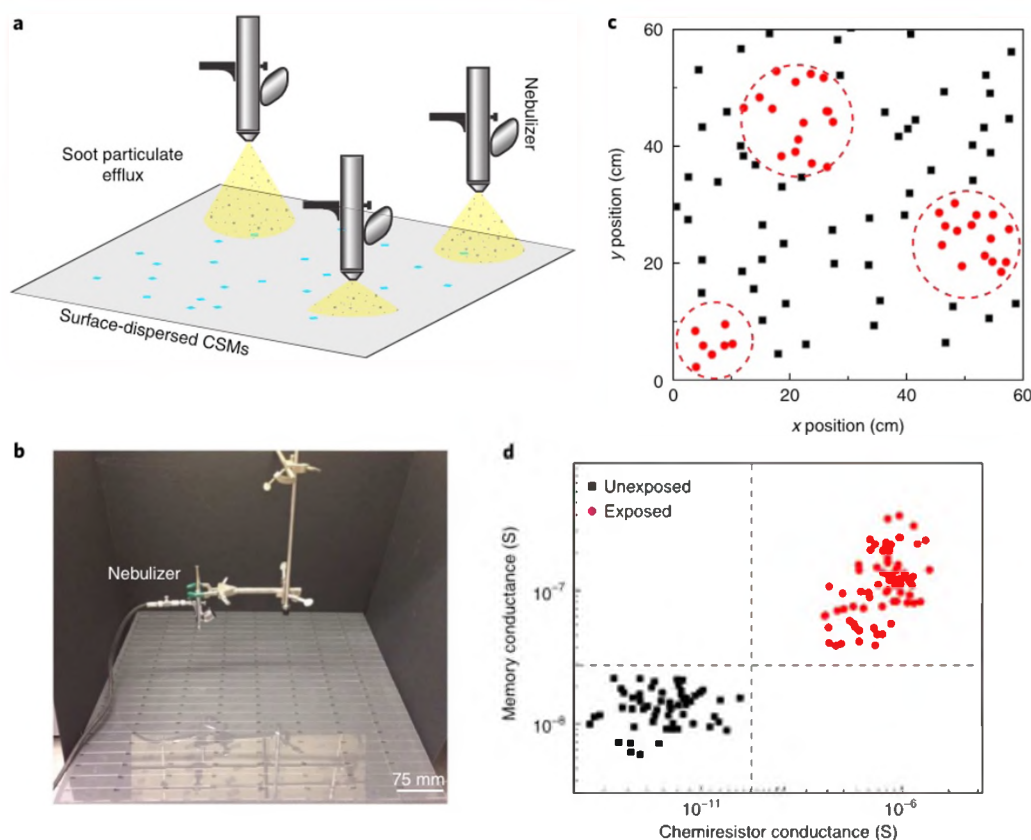


Fig. 5 | Large-area sensing. **a.** Schematic of set-up. Soot particles are sprayed at three locations over an area with previously dispersed CSMs (teal squares). **b.** Image of experimental set-up. **c.** Digitized positions of aerosolized CSMs. Dashed circles are guides for the eye, highlighting three areas exposed to soot. **d.** Chemiresistor conductance changes due to CSM exposure to soot, enabling memory conductance changes after illumination with a 532 nm laser ($7 \mu\text{W} \mu\text{m}^{-2}$).

during their initial runs, demonstrate excellent retention over a period of 2 h (Supplementary Fig. 13). Both the threshold voltage $V_{th} = 0.17 \pm 0.02 \text{ V}$ and initial conductance $= 14.4 \pm 6.9 \text{ nS}$ for aerosolized devices are similar to those for the on-substrate devices (Fig. 2l).

Once assembled, operation of the CSM requires that the photodiode voltage ε exceed the threshold memristor voltage V_{th} . The second criterion is that the memristor should not change its state if there is only analyte detection. To this end, we shielded all circuit elements except for the chemiresistor sensor using hBN monolayers (Supplementary Fig. 3). The memristor should also not change state with only light excitation; hence, the chemiresistor design includes an initial conductance G_{ch}^{in} , such that the voltage generated across the memristor does not exceed V_{th} . This sets the lower limit for the initial chemiresistance ($R_{ch}^{in} = 1/G_{ch}^{in}$), which can be determined by Ohm's law as

$$R_{ch}^{in} > R_m^{off} \left(\frac{\varepsilon}{V_{th}} - 1 \right) - R_{ph} \quad (3)$$

where R_{ph} is the photodiode resistance. After chemical detection via reaction with the analyte, the chemiresistor decreases its resistance to R_{ch}^{on} . This allows the memristor to change its state from R_m^{off} to R_m^{on} , which again can be assessed through the Ohm's law:

$$R_m^{on} = \frac{R_{ch}^{on} + R_{ph}}{\frac{\varepsilon}{V_{th}} - 1} \quad (4)$$

For the memristor to change its state, $< R_m^{off}$, has to be satisfied, yielding

$$R_{ch}^f < R_m^{off} \left(\frac{\varepsilon}{V_{th}} - 1 \right) - R_{ph} \quad (5)$$

Equations (3) and (5) set the requirements for the circuit design, so we had to carefully tune MoS_2 size (Supplementary Note 6).

The use of 2D materials keeps the particle aspect ratio α close to that of the bare substrate. This, in turn, leads to higher particle buoyancy, which approaches the values of water droplets in clouds (Supplementary Note 4). Sedimentation speed increases with particle size L and with α and ρ_p (Supplementary Fig. 14). For CSMs made of SU-8 bases, $\rho_p = 1,200 \text{ kg m}^{-3}$, $L = 50 \mu\text{m}$ and $\alpha = 0.01$, the sedimentation speed is $\sim 20 \mu\text{m s}^{-1}$, allowing them to stay in the air for days. To achieve similar result, silicon particles ($\rho_p = 2,300 \text{ kg m}^{-3}$) with conventionally thicker electronics ($\alpha = 0.1$) have to be as small as $5 \mu\text{m}$.

Aerosolizable electronics

Large-area monitoring of bacteria, spores, smoke particles, dust components and VOCs is an important objective, which currently requires significant resources¹⁹. In one implementation, satellite scanning can rapidly cover large areas, but is costly and indirect (with limited applicability)³⁸. On-ground sensor installation and networking is labour-intensive and can often be slow in comparison to analyte distribution³⁸. Using a fleet of aerial sensors (such as unmanned air vehicle drones) is again associated with high costs.

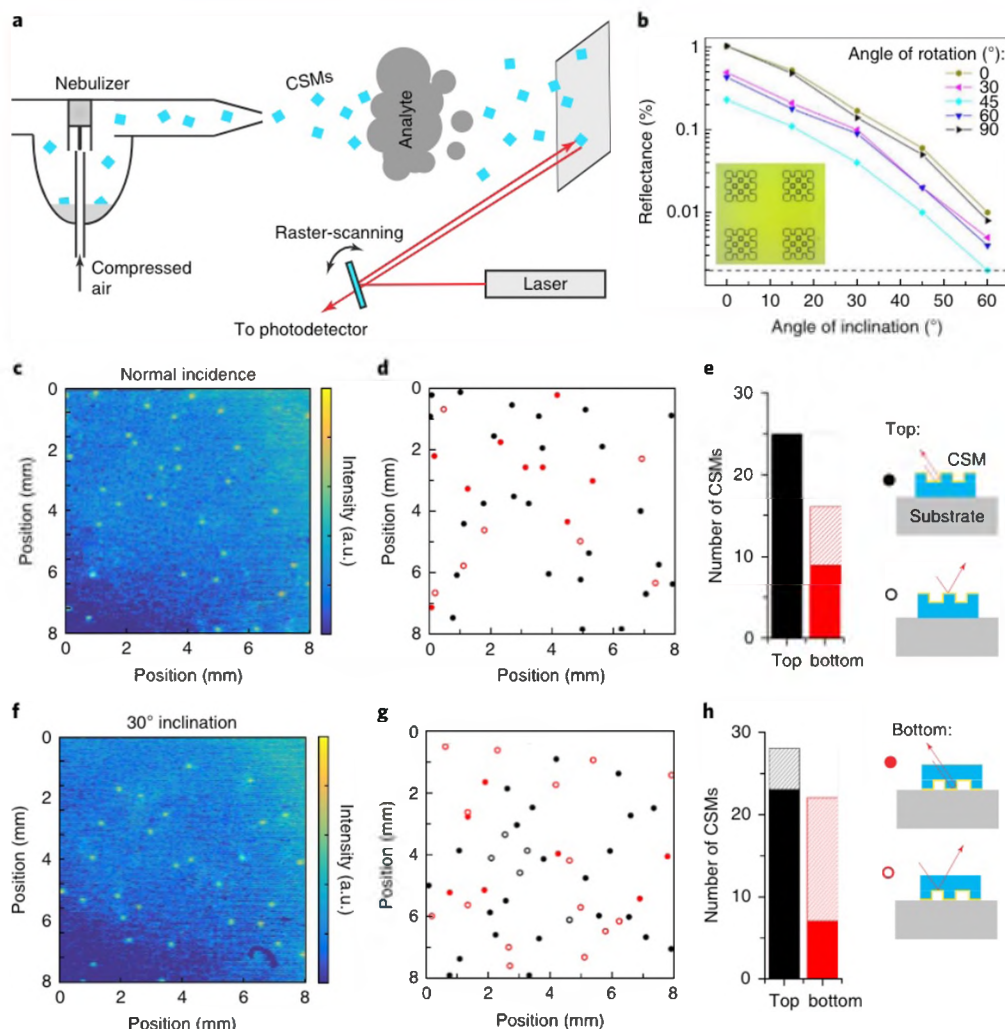


Fig. 6 | CSM standoff detection. **a**, CSMs are sprayed using a nebulizer through 10 mM TEA or 2 mg l⁻¹ soot dispersed in air. A raster-scanning laser system is then used to find CSMs. **b**, Retroreflector-CSM reflectance as a function of inclination and rotational angles. The dashed line marks the diffuse reflection limit $2 \times 10^{-3}\%$. Inset, Top view of 100 μm retroreflectors. **c**, Laser raster-scanning detection of 100 μm CSMs that landed after spraying. **d**, CSM positions extracted under a microscope: black circles, CSMs with retroreflectors on top; red circles, CSMs with flipped retroreflectors; open circles, CSMs that were not detected by the laser scan in **c**. **e**, Statistics on CSMs. Schematics on the right demonstrate figure labels. **f–h**, As in **c–e**, but for 30° substrate inclination angle.

As an alternative, we introduce the concept of aerosolizable electronics: CSMs dispersed in air carry 2D electronic devices that remain operational during and after flight.

To demonstrate the state machine operations, we fabricated CSMs with three components assembled in one closed circuit (Fig. 1a) and tested them (1) as fabricated on the silicon substrate and (2) on spraying in air within a confined chamber (Fig. 3a,b; see Methods). On exposure to 10 mM TEA, the sprayed CSMs change their chemiresistor conductance from $8.9 \pm 3.1 \text{ nS}$ to $G_{\text{ch}}^{\text{f}} = 17.3 \pm 4.1 \text{ nS}$ (consistent with Fig. 2h), allowing a memristor conductance change from $G_{\text{m}}^{\text{off}} = 13.3 \pm 4.8 \text{ nS}$ to $G_{\text{m}}^{\text{on}} = 17.3 \pm 8.9 \text{ nS}$ after laser illumination (two-tailed $P = 0.0001$, $N = 100$, Fig. 3c). We obtained similar results for CSMs on substrate: 59 CSMs successfully changed their states, with an average memory conductance ratio of 1.5 (Fig. 3e,g and Supplementary Fig. 15).

The chemiresistor sensor works better with larger conductive changes following analyte detection, and this is an area for future improvement. For example, if we use conductive carbon nanotubes dispersed at 0.2 g l^{-1} as the analyte, the detection efficiency increases substantially. For these experiments we used an insulating substrate (SU-8, sheet resistance $\sim 10 \text{ pS}$) instead of the MoS_2 as

the chemiresistor, increasing $R_{\text{ch}}^{\text{in}}$. Adsorbed carbon nanotubes form a percolated network with conductivities on the order of μS (Supplementary Fig. 16), providing high gain to better satisfy equation (5). In a typical experiment, sprayed CSMs change their chemiresistor conductance from $G_{\text{ch}}^{\text{in}} = 8.7 \pm 2.0 \text{ pS}$ to $G_{\text{ch}}^{\text{f}} = 4.3 \pm 2.7 \mu\text{S}$, inducing a memristor change from $G_{\text{m}}^{\text{off}} = 14.7 \pm 6.0 \text{ nS}$ to $G_{\text{m}}^{\text{on}} = 0.47 \pm 0.44 \mu\text{S}$ with 71 active CSMs (Fig. 3d), with similar performance for on-substrate CSMs (Fig. 3f,h).

Demonstration of constrained environmental sensing

Researchers have identified several important closed systems from which it is difficult to extract information or interface electronics within an inaccessible interior¹⁹. Examples include oil and gas conduits^{40,41}, chemical and biosynthetic reactors^{42,43}, porous geological materials for upstream oil and mining exploration^{44,45} and the human digestive tract^{46,47}. Several methods to probe such systems exist, but they are either indirect or very limited in their applicability (Supplementary Note 7). At the same time, fully autonomous electronic chips have been limited to the millimetre scale^{46,48}, which is too large to address the above applications. To this end, we demonstrate that CSMs can be injected into a

pipeline system, probe it, and then be successfully retrieved to deliver the captured information.

To illustrate, a model pipeline section was fabricated, into which gaseous ammonia was injected. Ammonia is a highly toxic gas used as a fertilizer in agriculture and as a refrigerant in the chemical industry¹⁹. It is also one of the most dangerous compounds to be transported through pipelines⁵⁰. To probe the pipeline internally, we first injected CSMs within the system (Fig. 4a) as a nebulized aerosol. A valve was then used to pulse ammonia vapour (~10 kPa) into the system, allowing the CSMs to interact with it for 30 min. Next, the ammonia valve was closed and the CSMs retrieved from the collector (Fig. 4b,c). The experimental procedure is similar to the previous section, with some CSMs inserted into the tube on-substrate as a control. Ammonia vapour acts as an n-dopant for the MoS₂ layer³¹, changing MoS₂ conductances from $G_{\text{ch}}^{\text{in}} = 9.1 \pm 2.2 \text{ nS}$ to $G_{\text{ch}}^{\text{f}} = 18.5 \pm 2.5 \text{ nS}$ for the sprayed CSMs and, consequently, allowing a memristor conductance change from $G_{\text{m}}^{\text{off}} = 12.5 \pm 3.9 \text{ nS}$ to $G_{\text{m}}^{\text{on}} = 14.5 \pm 4.3 \text{ nS}$ after laser illumination (two-tailed $P = 0.0007$, $N = 100$, Fig. 4d) with similar results for the on-substrate CSMs (Fig. 4e,f and Supplementary Fig. 17).

State machines for soot exposure monitoring

Soot nanoparticles emitted by diesel engines, industrial emissions and power plants pose health, climate and environmental risks⁵². Aerosolized micro- and nanoparticles can travel thousands of kilometres before sedimentation⁵³, making it challenging to predict soot distribution and impact. Currently, the large-area monitoring of soot remains an economically inviable task. To this end, CSMs as dispersed, printed devices can potentially cover large areas to successfully detect soot, remaining virtually invisible to the naked eye, but otherwise easily detectable on a surface (see next paragraph). In this case, aerosolization allows CSMs to be rapidly printed over a specific area of interest as intact, functional, autonomously powered devices.

To demonstrate the monitoring of undesirable particulates from surface-dispersed CSMs, the nebulized CSMs were deposited over an area of $0.6 \times 0.6 \text{ m}^2$. Next, 2 g l^{-1} of Printex XE2-B soot was loaded into a separate nebulizer and sprayed over three distinct locations (Fig. 5a,b and Supplementary Fig. 18), simulating localized particulate efflux. For these experiments we used an insulating substrate (SU-8, sheet resistance ~10 pS) instead of MoS₂ as the CSM chemiresistor. The remainder of the experimental procedure is similar to previous experiments. By their nature, soot particles are highly conductive⁵⁴; thus, the chemiresistor element drastically changes its conductance from $G_{\text{ch}}^{\text{in}} = 7.4 \pm 2.4 \text{ pS}$ to $G_{\text{ch}}^{\text{f}} = 0.80 \pm 0.26 \mu \text{ S}$ on exposure to soot. This further translates into memristor conductance changes from $G_{\text{m}}^{\text{off}} = 13.7 \pm 4.2 \text{ nS}$ to $G_{\text{m}}^{\text{on}} = 127 \pm 72 \text{ nS}$ following laser illumination (Fig. 5d). The retrieved CSM positions allow determination of the exposed and unexposed areas (Fig. 5c).

Enhancements of state machines to aid standoff detection

To efficiently detect the location of CSMs at standoff distances, we fabricated a distinct batch, where the CSM batch consisted of a retroreflector design. The design follows that of Switkes et al.⁵⁵ with a 100 μm retroreflector for low-intensity laser (10 mW cm^{-2}) reflected light from distances of up to 1 km (ref. ⁵⁵). CSM retroreflectors were fabricated using SU-8 coated with 100 nm Ag, designed in a chequered shape, that allows them to reflect light back to the source from angles up to 60° (Fig. 6b). We used a custom laser-scanning system (Fig. 6a) to rapidly scan (<1 ms) and detect reflection from CSMs that landed after spraying over an $8 \times 8 \text{ mm}^2$ area at a 5 cm standoff distance (Fig. 6c). Careful examination under a microscope showed that $N = 34$ CSMs were detected (Fig. 6d,e): 25 CSMs (100% refers to the percentage of CSMs detected by laser scanning versus the total number of CSMs identified under the microscope for a given category) had their reflectors facing up and $N = 9$ (56%) were flipped. The yield becomes slightly lower for CSM detection on an

inclined substrate due to imperfect backreflections (Fig. 6f–h): 23 CSMs (82%) were facing up and 7 CSMs (32%) were flipped. These results suggest that this attribute of CSMs can aid in their tracking and recovery over large areas, and, with refinement, could increase the detection threshold to 100% with a $10 \text{ cm}^2 \text{ s}^{-1}$ scan.

We have demonstrated the capability of grafting autonomous electronic circuits capable of logic operation and information storage on submillimetre-sized particles, forming CSMs. Our particles can undergo aerosolization while carrying functional electronics on-board capable of interaction with the environment. With a thickness of $1.24 \mu \text{m}$ and weight of $\sim 1.4 \text{ g m}^{-2}$, this CSM design represents one of the thinnest and lightest circuits produced so far²⁷. In this design, the on-board circuit forms a state machine with two inputs (chemical and optical) and one output composed of a memristor. Due to the use of 2D materials, CSM requires only 30 nW to irreversibly record events, granting it the ability to be powered from the energy harvested by the on-board 2D photodiode (30–100 nW). The results of chemical sensing are irreversibly stored in the memory (inducing memristor conductivity changes of up to 150 times). Furthermore, the addition of integrated retroreflectors allows the dispersed CSMs to be rapidly (<1 ms per frame) detected by a laser-scanning system. CSMs may find application in a wide range of areas, including biosensing (for example, within the human digestive tract), large-area sensing, confined space monitoring (for example, chemical and biosynthetic reactors, oil and gas conduits) and aerospace programmes.

Methods

Methods, including statements of data availability and any associated accession codes and references, are available at <https://doi.org/10.1038/s41565-018-0194-z>.

Received: 23 October 2017; Accepted: 11 June 2018;

Published online: 23 July 2018

References

- Lou, Z., Liang, Z. & Shen, G. Photodetectors based on two dimensional materials. *J. Semicond.* **37**, 091001 (2016).
- Chhowalla, M., Jena, D. & Zhang, H. Two-dimensional semiconductors for transistors. *Nature* **1**, 16052 (2016).
- Varghese, S., Varghese, S., Swaminathan, S., Singh, K. & Mittal, V. Two-dimensional materials for sensing: graphene and beyond. *Electronics* **4**, 651 (2015).
- Yuan, J. & Lou, J. 2D materials: memristor goes two-dimensional. *Nat. Nanotech.* **10**, 389–390 (2015).
- Zhang, X., Hou, L., Ciesielski, A. & Samori, P. 2D materials beyond graphene for high-performance energy storage applications. *Adv. Energy Mater.* **6**, 1600671 (2016).
- Khorasani, S. & Koottandavida, A. Nonlinear graphene quantum capacitors for electro-optics. *2D Mater. Appl.* **1**, 7 (2017).
- Kaewsancha, C., Tangboriboonrat, P., Polpanich, D. & Elaissari, A. Multifunctional fluorescent-magnetic polymeric colloidal particles: preparations and bioanalytical applications. *ACS Appl. Mater. Interfaces* **7**, 23373–23386 (2015).
- Kamaly, N., Yameen, B., Wu, J. & Farokhzad, O. C. Degradable controlled-release polymers and polymeric nanoparticles: mechanisms of controlling drug release. *Chem. Rev.* **116**, 2602–2663 (2016).
- Udo, S. Stochastic thermodynamics, fluctuation theorems and molecular machines. *Rep. Progress Phys.* **75**, 126001 (2012).
- Velegol, D. Assembling colloidal devices by controlling interparticle forces. *Proc. SPIE* **1**, 25 (2007).
- Spellings, M. et al. Shape control and compartmentalization in active colloidal cells. *Proc. Natl Acad. Sci. USA* **112**, 4642 (2015).
- Yao, J. et al. Nanowire nanocomputer as a finite-state machine. *Proc. Natl Acad. Sci. USA* **111**, 2431–2435 (2014).
- Ding, T. et al. Light-induced actuating nanotransducers. *Proc. Natl Acad. Sci. USA* **113**, 5503–5507 (2016).
- Funke, D. A. et al. A 200 μm by 100 μm smart dust system with an average current consumption of 1.3 nA. *IEEE Proc. ICECS 2016* **1**, 512–515 (2016).
- Taniguchi, M. & Kawai, T. DNA electronics. *Physica E* **33**, 1–12 (2006).
- Siuti, P., Yazbek, J. & Lu, T. K. Engineering genetic circuits that compute and remember. *Nat. Protoc.* **9**, 1292–1300 (2014).

17. Kamm, R. D. & Bashir, R. Creating living cellular machines. *Ann. Biomed. Eng.* **42**, 445–459 (2014).
18. Roquet, N., Soleimany, A. P., Ferris, A. C., Aaronson, S. & Lu, T. K. Synthetic recombinase-based state machines in living cells. *Science* **353**, aad8559 (2016).
19. Hansen, M. C. & Loveland, T. R. A review of large area monitoring of land cover change using Landsat data. *Remote Sens. Environ.* **122**, 66–74 (2012).
20. Seo, D. et al. Wireless recording in the peripheral nervous system with ultrasonic neural dust. *Neuron* **91**, 529–539 (2016).
21. Ferrari, S. et al. Latest advances in the manufacturing of 3D rechargeable lithium microbatteries. *J. Power Sources* **286**, 25–46 (2015).
22. Seo, D., Carmena, J. M., Rabaey, J. M., Maharbiz, M. M. & Alon, E. Model validation of untethered, ultrasonic neural dust motes for cortical recording. *J. Neurosci. Methods* **244**, 114–122 (2015).
23. Kim, H. & Kim, M. J. Electric field control of bacteria-powered microrobots using a static obstacle avoidance algorithm. *IEEE Trans. Robot.* **32**, 125–137 (2016).
24. Servant, A., Qiu, F., Mazza, M., Kostarelos, K. & Nelson, B. J. Controlled in vivo swimming of a swarm of bacteria-like microrobotic flagella. *Adv. Mater.* **27**, 2981–2988 (2015).
25. Ionescu, A. M. & Riel, H. Tunnel field-effect transistors as energy-efficient electronic switches. *Nature* **479**, 329–337 (2011).
26. Fiori, G. et al. Electronics based on two-dimensional materials. *Nat. Nanotech.* **9**, 768–779 (2014).
27. Salvatore, G. A. et al. Wafer-scale design of lightweight and transparent electronics that wraps around hairs. *Nat. Commun.* **5**, 2982 (2014).
28. Akinwande, D., Petrone, N. & Hone, J. Two-dimensional flexible nanoelectronics. *Nat. Commun.* **5**, 5678 (2014).
29. Fang, H. et al. Strong interlayer coupling in van der Waals heterostructures built from single-layer chalcogenides. *Proc. Natl Acad. Sci. USA* **111**, 6198–6202 (2014).
30. Cheng, R. et al. Electroluminescence and photocurrent generation from atomically sharp WSe₂/MoS₂ heterojunction p–n diodes. *Nano Lett.* **14**, 5590–5597 (2014).
31. Ye, L., Li, H., Chen, Z. & Xu, J. Near-infrared photodetector based on MoS₂/black phosphorus heterojunction. *ACS Photon.* **3**, 692–699 (2016).
32. Perkins, F. K. et al. Chemical vapor sensing with monolayer MoS₂. *Nano Lett.* **13**, 668–673 (2013).
33. Mouri, S., Miyauchi, Y. & Matsuda, K. Tunable photoluminescence of monolayer MoS₂ via chemical doping. *Nano Lett.* **13**, 5944–5948 (2013).
34. Hao, C. et al. Liquid-exfoliated black phosphorous nanosheet thin films for flexible resistive random access memory applications. *Adv. Funct. Mater.* **26**, 2016–2024 (2016).
35. Wang, W. et al. MoS₂ memristor with photoresistive switching. *Sci. Rep.* **6**, 31224 (2016).
36. Sangwan, V. K. et al. Gate-tunable memristive phenomena mediated by grain boundaries in single-layer MoS₂. *Nat. Nanotech.* **10**, 403–406 (2015).
37. Bessonov, A. A. et al. Layered memristive and memcapacitive switches for printable electronics. *Nat. Mater.* **14**, 199–204 (2015).
38. Lillesand, T., Kiefer, R. W. & Chipman, J. in *Remote Sensing and Image Interpretation* 1–59 (Wiley, New York, NY, 2014).
39. Brunete, A., Hernando, M., Torres, J. E. & Gambao, E. Heterogeneous multi-configurable chained microrobot for the exploration of small cavities. *Autom. Constr. Magaz.* **21**, 184–198 (2012).
40. Muravy, P.-S. & Silea, I. A survey on gas leak detection and localization techniques. *J. Loss Prev. Process Ind.* **25**, 966–973 (2012).
41. Rajtar, J. M. & Muthiah, R. Pipeline leak detection system for oil and gas flowlines. *J. Manufact. Sci. Eng.* **119**, 105–109 (1997).
42. Gavrilescu, M. & Tudose, R. Z. Residence time distribution of the liquid phase in a concentric-tube airlift reactor. *Chem. Eng. Process.* **38**, 225–238 (1999).
43. Kurt, S. K., Gelhausen, M. G. & Kockmann, N. Axial dispersion and heat transfer in a milli/microstructured coiled flow inverter for narrow residence time distribution at laminar flow. *Chem. Eng. Tech.* **38**, 1122–1130 (2015).
44. Tan, X., Sun, Z. & Akyildiz, I. F. Wireless underground sensor networks: MI-based communication systems for underground applications. *IEEE Antennas Propag.* **57**, 74–87 (2015).
45. Yamate, T., Fujisawa, G. & Ikegami, T. Optical sensors for the exploration of oil and gas. *J. Light. Technol.* **35**, 3538–3545 (2017).
46. Kalantar-Zadeh, K. et al. A human pilot trial of ingestible electronic capsules capable of sensing different gases in the gut. *Nat. Electron.* **1**, 79–87 (2018).
47. Costello, B. P. J. d. L., Ledochowski, M. & Ratcliffe, N. M. The importance of methane breath testing: a review. *J. Breath. Res.* **7**, 024001 (2013).
48. Farra, R. et al. First-in-human testing of a wirelessly controlled drug delivery microchip. *Sci. Transl. Med.* **4**, 122ra21 (2012).
49. Timmer, B., Olthuis, W. & Berg, A. Ammonia sensors and their applications—a review. *Sens. Actuat. B* **107**, 666–677 (2005).
50. Nielsen, A. (ed.) in *Ammonia: Catalysis and Manufacture* (ed. Nielsen, A.) 329–346 (Springer, Berlin, 1995).
51. Cho, B. et al. Charge-transfer-based gas sensing using atomic-layer MoS₂. *Sci. Rep.* **5**, 8052 (2015).
52. Bernstein, J. A. et al. Health effects of air pollution. *J. Allergy Clin. Immunol.* **114**, 1116–1123 (2004).
53. Derbyshire, E. Natural minerogenic dust and human health. *AMBIO* **36**, 73–77 (2007).
54. Grob, B., Schmid, J., Ivleva, N. P. & Niessner, R. Conductivity for soot sensing: possibilities and limitations. *Anal. Chem.* **84**, 3586–3592 (2012).
55. Switkes, M., Ervin, B. L., Kingsborough, R. P., Rothschild, M. & Sworin, M. Retroreflectors for remote readout of colorimetric sensors. *Sens. Actuat. B* **160**, 1244–1249 (2011).

Acknowledgements

This work was funded by a 2015 US Office of Naval Research Multi University Research Initiative (MURI) grant on Foldable and Adaptive Two-Dimensional Electronics (FATE) at MIT, Harvard and University of Southern California. V.B.K. is supported by The Swiss National Science Foundation (projects nos P2ELP3_162149 and P300P2_174469). Microfabrication for this work was performed at the Harvard University Center for Nanoscale Systems (CNS), a member of the National Nanotechnology Coordinated Infrastructure Network (NNCI), which is supported by the National Science Foundation under NSF award no. 1541959. D.K. is supported by a Grant-in-Aid for JSPS Fellows (JSPS KAKENHI grant no. 15J07423) and Encouragement of Young Scientists (B) (JSPS KAKENHI grant no. JP16K17485) from the Japan Society for the Promotion of Science.

Author contributions

V.B.K. and M.S.S. conceived the idea and planned experiments with the assistance of P.L., D.K. and A.T.L. V.B.K. fabricated samples, performed experimental measurements, and analysed data with the assistance of P.L. and D.K. V.B.K. and J.A.L. fabricated 2D materials with inputs from Y.S., P.L. and D.K. V.B.K., A.L.C. and M.S.S. wrote the manuscript with inputs from all the authors. All authors contributed to discussions informing the research.

Competing interests

The authors declare no competing interests.

Additional information

Supplementary information is available for this paper at <https://doi.org/10.1038/s41565-018-0194-z>.

Reprints and permissions information is available at www.nature.com/reprints.

Correspondence and requests for materials should be addressed to M.S.S.

Publisher's note: Springer Nature remains neutral with regard to jurisdictional claims in published maps and institutional affiliations.

Methods

2D materials. Large-area MoS_2 films were grown by a chemical vapour deposition process as described elsewhere²⁴. Briefly, solid 0.5 g S and 4 mg MoCl_5 were used as precursors, and a $2 \times 1 \text{ cm}^2$ 300 nm SiO_2/Si wafer piece was used as a growth substrate in a vacuum tube quartz furnace. The system was filled with 50 s.c.c.m. Ar for 1 h with subsequent growth at 850 °C under 2 torr pressure for 10 min and a 30 min temperature ramp. As-grown MoS_2 films were coated with polystyrene and peeled from the substrate, taking advantage of the surface-energy-assisted method²⁵. Continuous films of hBN and WSe₂ monolayers were purchased from Graphene Supermarket and 6Carbon, respectively.

Characterization. Raman and photoluminescence measurements were performed using a Raman spectrometer HR-800 (Horiba BY) with 532 nm laser. Height profiles were measured using a CCI HD optical profiler. Electrical resistance measurements were performed in an ARS PSF-10-1-4 Cryogenic Probe Station using micromanipulators as probes (7×, Micromanipulator). Conductance measurements were performed by scanning the voltage from -0.1 to 0.1 V. Particle size distribution was measured using a nanoparticle tracking LM-10 Nanosight (Malvern).

CSM fabrication. To define polymer CSM bases, the first photolithography step was performed using the negative photoresist SU-8 2002 on SiO_2/Si wafer (Supplementary Fig. 2). Next, a monolayer of MoS_2 (patterned in 25- μm -wide stripes using oxygen etching) with a PMMA support layer was transferred onto the structure with subsequent annealing at 80 °C for 1 h and 150 °C for 30 min. The wafer was then washed in acetone and ethanol and dried under nitrogen to remove the PMMA layer. In parallel, a monolayer of WSe₂ was prepared on a separate wafer: 25- μm -wide WSe₂ stripes were defined using the second photolithography step with the positive photoresist Shipley S1805 and subsequent oxygen etching. The photoresist was removed in RemoverPG developer. The patterned WSe₂ monolayer was then transferred onto MoS_2 using PMMA as the support layer, annealed at 80 °C for 1 h and 150 °C for 30 min. The wafer was washed in acetone and ethanol and dried under nitrogen. The third photolithography with a LOR30B sacrificial layer and a positive photoresist Shipley S1805 was used to define 40-nm-thick gold electrical contacts, which were deposited using a Denton electron-beam evaporator. The liftoff process was performed in Remover PG at 80 °C.

The fourth photolithography step with a LOR30B sacrificial layer and Shipley S1805 was used to define the structure of a subsequent MoS_2 film. The MoS_2 film was deposited using a modified Langmuir–Blodgett method, where the MoS_2 film was collected at an ethanol–hexane interface²⁷. To form the top oxide layer, the structure was annealed at 200 °C for 2 h. The liftoff process was performed in Remover PG at 80 °C. The fifth photolithography with a LOR30B sacrificial layer and Shipley S1805 was used to define 100-nm-thick silver electrical contacts. The liftoff process was performed in Remover PG at 80 °C. Monolayer hBN (patterned in 50- μm -wide stripes) was then transferred on top. Because hBN is transparent, its alignment on the CSM is very challenging. To this end, we transferred hBN with S1850 photoresist to help visualize the structure (the photoresist was removed

afterwards). Finally, CSMs were coated with a PMMA layer for support and lifted off the substrate using KOH solution. To disperse CSMs, the PMMA was dissolved in acetone.

Retroreflectors were fabricated using SU-8 photolithography with subsequent evaporation of 100 nm silver.

Soot experiments. We used commercially available Printex XE2-B soot. To make aerosol, we dispersed 2 mg of soot with 4 mg of BSA in 1 ml of deionized water. The mixture was sonicated with a 1/8"-inch probe tip at 40% amplitude (~ 12 W) for 30 min in an ice bath. For aerosol experiments, the mixture was diluted by 1,000×. Soot aggregates in the absence of the surfactant, inhomogeneously covering CSMs and blocking photodetectors.

Aerosol experiments. All aerosol experiments were performed with a Master Airbrush G22 nebulizer in a closed tube in the laminar flow hood. CSMs (dispersed in 80% water/20% ethanol) were sprayed under 2–15 psi pressure from a 300 μm nozzle. The second nebulizer was used to spray analyte droplets in the orthogonal direction (Supplementary Fig. 4). Aggregated CSMs, CSMs with visual defects, and CSMs that landed upside down were excluded from analysis.

In a typical experiment, a portion of dispersed CSMs is pipetted onto the silicon substrate and is left to dry until all water evaporates naturally. Next, we query the initial CSM state with a probe station: both the memristor behaviours and the chemiresistor conductances on $N = 100$ CSMs are measured. The remainder of the CSMs are sprayed across in an enclosed tube. TEA is continuously sprayed using the second nebulizer from the top of the tube starting 5 s before and ending immediately after the CSMs are sprayed across (to eliminate interference of the two flows). CSMs are then left for 1 h inside to react with TEA and dry. We then place CSMs under the microscope and illuminate every photodiode individually for 5 s (532 nm laser, $7 \mu\text{W} \mu\text{m}^{-2}$). Next, the final state of CSMs is assessed ($N = 100$), repeating the same measurements as for the initial state. While for sprayed experiments these are random CSMs, we identify CSMs for on-substrate experiments, extracting individual changes on every CSM.

Standoff detection. Standoff CSM detection was performed using a set-up with galvanized mirrors, a 532 nm laser, and a photodetector (H10330a-25, Hamamatsu).

Data availability. The data that support the plots within this paper and other findings of this study are available from the corresponding author upon reasonable request.

References

56. Yu, Y. et al. Controlled scalable synthesis of uniform, high-quality monolayer and few-layer MoS_2 films. *Sci. Rep.* **3**, 1866 (2013).
57. Gurarslan, A. et al. Surface-energy-assisted perfect transfer of centimeter-scale monolayer and few-layer MoS_2 films onto arbitrary substrates. *ACS Nano* **8**, 11522–11528 (2014).